Phys Chem Minerals (2011) 38:435–448
DOI 10.1007/s00269-011-0417-4

ORIGINAL PAPER

Polytype and polymorph identification of finely divided aluminous dioctahedral mica individual crystals with SAED. Kinematical and dynamical electron diffraction

Anne-Claire Gaillot · Victor A. Drits · David R. Veblen · Bruno Lanson

Received: 21 July 2010 / Accepted: 18 January 2011 / Published online: 12 February 2011

Abstract This work investigates the potential of selected-area electron diffraction (SAED) for the polytype and polymorph identification of finely divided K-bearing aluminous dioctahedral mica. Individual mica crystals may indeed differ by their layer-stacking sequence and by the inner structure of their octahedral sheets (polytypic and polymorphic variants, respectively). This diversity of natural mica is commonly considered to be responsible for their morphological variety. The present article thus analyzes the intensity distribution between *hk*0 beams as a function of the crystal structure and thickness. The comparison of ED calculations with experimental diffraction data shows that predicted dynamical effects are not observed for finely divided dioctahedral mica. The influence of different structure defects on calculated intensities is analyzed, and their widespread occurrence in natural mica is hypothesized to be responsible for the limitation of dynamical diffraction effects. SAED may thus be used to identify the structure of individual dioctahedral mica crystals using the kinematical approximation to simulate and qualitatively interpret the observed intensities.

Keywords Electron diffraction · Dioctahedral mica · Polymorph · Polytype · Cis-vacant · Trans-vacant · Illite · Muscovite · Dynamical diffraction · Kinematical approximation

Electronic supplementary material The online version of this article (doi:10.1007/s00269-011-0417-4) contains supplementary material, which is available to authorized users.

A.-C. Gaillot (✉)
Institut des Matériaux Jean Rouxel (IMN),
Université de Nantes, CNRS, 2 rue de la Houssinière,
BP 32229, 44322 Nantes Cedex 3, France
e-mail: Anne-Claire.Gaillot@cnrs-imn.fr

A.-C. Gaillot · D. R. Veblen
Morton K. Blaustein Department of Earth and
Planetary Sciences, Johns Hopkins University,
Baltimore, MD 21218, USA

V. A. Drits
Geological Institute of Russian Academy of Sciences,
Pyzhevsky per. 7, 109017 Moscow, Russia

B. Lanson
ISTerre, Maison des Géosciences, CNRS–University
of Grenoble, 38041 Grenoble Cedex 9, France

Introduction

Finely divided dioctahedral 2:1 (TOT) phyllosilicates from the mica family are ubiquitous in a wide range of geological environments and occur as sub-micron size particles with structural variants known as polytypes and polymorphs (Bailey 1984). Mica polytypes differ by the stacking sequence of their TOT layers (1*M*, $2M_1$, $2M_2$, 2*O*, 3*T*), whereas polymorphs differ by the location of the vacancy within the dioctahedral aluminous sheet [*cis*-vacant (cv) or *trans*-vacant (tv)]. Different structural variants commonly coexist, even at the small scale, but little is known about the factors responsible for the formation of a given variant.

Over the last decades, techniques were developed to determine and/or identify these mica structures in pure specimens or mixtures. In particular, powder X-ray diffraction (XRD) and oblique-texture electron diffraction (OTED) have been widely used (the latter essentially in the former USSR owing to specific technical requirements) to determine the structure of mica polytypes crystallizing in different space groups with different unit-cell parameters (Zvyagin 1967; Drits et al. 1984a, 1993, 1998, 2006; Weiss

and Wiewiora 1986; Bailey 1988; Durovic 1992; Drits and Sakharov 2004; Zviagina et al. 2007). For XRD, criteria based on the interpretation of the intensity variation along specific rods (20*l* and 02*l*) or on thorough comprehensive analysis of line positions were established allowing differentiation of mica polytypes and polymorphs. Differential thermal analysis (DTA) was also shown to be an efficient technique to discriminate cv and tv polymorphs from their respective dehydroxylation temperatures (Drits et al. 1998; Emmerich et al. 1999; Emmerich and Kahr 2001). But both XRD and DTA provide only statistical information on the whole crystal population, and no relationship between crystal shape, chemical composition and structure can be established. Because crystal habits, and possibly crystal chemistry, were shown to be statistically correlated to crystal structure (Lanson et al. 1996, 2002; Patrier et al. 2003; Laverret et al. 2006), it is of interest to determine the polytype and polymorph of single crystals, that is, not only the stacking sequence of their TOT layers but also the detailed structure of their dioctahedral sheet.

Electron microscopy appears as an obvious tool for this purpose as it allows probing individual crystals in a complex mixture. Electron back-scattered diffraction (EBSD) technique in a scanning electron microscope can be an efficient tool for studying phyllosilicates polytypes (Kogure 2002a). However, this technique requires large and thick crystals and is therefore not adapted for studying finely divided dioctahedral mica. High-resolution transmission electron microscopy (HRTEM) allows distinguishing mica polytypes when crystals are observed with the electron beam parallel to the crystal layers by imaging at the atomic scale the periodicity and interlayer displacements in the stacking sequences (Amouric et al. 1978, 1981; Amouric and Baronnet 1983; Kogure and Nespolo 1999; Kogure 2002b; Kameda et al. 2007; Kogure et al. 2008). However, very thin crystals of dioctahedral mica (tv-paragonite, tv-muscovite, tv-celadonite, tv- and cv-illites) may dehydroxylate under electron radiation before HRTEM images can be recorded (Kogure 2002b; Kogure and Drits 2010). Moreover, during the dehydroxylation of cv crystals octahedral cations migrate from occupied *trans*-sites into formerly vacant *cis*-sites, thus prohibiting a valid characterization. Under such conditions, electron diffraction (ED) could be used as an alternative to HRTEM to identify dioctahedral mica polytypes and polymorphs as selected-area ED (SAED) patterns from thin crystals provides the needed 3D structural information with a much reduced electron flux, thus minimizing thermally induced structural modifications. Few studies used SAED (Güven 1974a, b) and convergent beam ED (Beermann and Brockamp 2005) for the identification of phyllosilicate structure and space group. But the turbostratic stacking prevailing in montmorillonite, which was the main species investigated in these early studies, is likely responsible for the pessimistic conclusions reached as to the potential of ED to discriminate phyllosilicate polytypes and polymorphs. In contrast, dioctahedral mica possess well-defined layer-stacking sequences. The geometry of ED patterns is, however, similar for all mica polytypes and polymorphs, and ED intensities must be analyzed either (1) with SAED and comparison with dynamical diffraction calculations or (2) with precession ED technique (PED) so as to minimize multiple scattering effects (Gemmi and Nicolopoulos 2007; Nicolopoulos et al. 2007; Moeck and Rouvimov 2010). The latter technique is recent and not available on most TEMs. This work thus focuses on the potential of SAED as a tool for mica polytype identification. Former works recommend analyzing the intensity distribution along the 20*l* and 02*l* reciprocal rows, which are the most appropriate ones to discriminate the mica polytypes (Weiss and Wiewiora 1986; Durovic 1992). However, such crystal orientations are difficult to access in the TEM as they require specific and difficult sample preparation (resin inclusion of oriented preparation and ultra-microtome sectioning). In addition, diffraction differences arising from tv- and cv-polymorphic variants are not discussed in these studies. In this work, the potential of the more easily accessible [001] zone axis is investigated, as it should be more suitable for tv versus cv polymorphs discrimination, and still of a certain use for the polytype identification. Experimental SAED patterns along [001] axis obtained on mica specimens are thus compared with theoretical calculations performed both with the kinematical approximation and the dynamical theory of diffraction. Definition of qualitative identification criteria based on kinematical intensity distribution between *hk*0 reflections is then discussed.

Theoretical background

This section summarizes the basic theoretical notions and the necessary terminology used hereafter. Details can be found in classical textbooks. When traveling through the crystal, electrons interact both with the atoms nuclei and their electronic cloud through strong Coulombic forces and are elastically scattered with a Bragg angle related to interplanar distances in the crystal. The small proportion of inelastically scattered electrons contributes essentially to background intensity. The amplitude of the diffracted electron wave after a single scattering event is proportional to the product of (1) the structure factor, F, that is the Fourier transform of the electronic density in the unit cell, and (2) the shape factor, L, that is the Fourier transform of the crystal lattice.

Relaxation of diffraction conditions

For a perfect crystal of infinite dimensions, the interference function, L^2, corresponds to a Dirac function equal to zero except for Bragg angles (θ_B). In these "ideal" conditions, SAED patterns could not be observed as no reciprocal lattice (RL) node would intersect the Ewald sphere (ES). In practice, real crystals have finite dimensions, and L^2 maxima are broadened, thus inducing an elongation of RL nodes that intersects the ES even when Bragg's law is not precisely satisfied (angle $2\theta_B + \Delta 2\theta_B$—Fig. 1a). The distance between the RL node center and the ES is called excitation error *s*. In TEM studies, this effect is reinforced by the low ES curvature. As a consequence, the amplitude of diffracted waves is not negligible out of perfect Bragg conditions allowing diffraction patterns to be observed. The thinner the specimen, the larger the number of observable zero-order Laue zone (ZOLZ) reflections. However, the intensity of *hk*0 reflections located far out in the reciprocal space is strongly reduced owing to the bell-shaped profile of the shape factor (damping effect—Fig. 1a, b).

Validity of kinematical approximation

Ideally, the investigated single crystal is thin enough so that electrons are overwhelmingly scattered only once (kinematical approximation), and diffracted intensities are proportional to F^2, modulated by L^2. However, if the 3D-periodic single crystal is thicker than twice the electron mean free path in the material, the probability of multiple scattering increases and the dynamical theory of diffraction should be used to describe the amplitude of diffracted beams (Cowley 1992). The interpretation of the diffracted intensity thus depends on the specimen (electron mean free path) but also on the ED technique used.

For example, OTED patterns obtained from a set of finely divided crystals were successfully interpreted using kinematical approach allowing mica structure refinement (Zvyagin 1967; Zvyagin et al. 1979). Even proton positions were determined with an R-factor of ~6% (Tsipursky and Drits 1977; Drits et al. 1984b; Plançon et al. 1985). In this case, the variability of particle thicknesses and their mutual disorientation dramatically decrease dynamical effects from individual microcrystals. When using PED, only a few beams are excited at a time, thus minimizing multiple scattering, and intensities are then proportional to *F* (Gemmi and Nicolopoulos 2007; Nicolopoulos et al. 2007; Moeck and Rouvimov 2010). However, the situation is not as clear for SAED and a thorough assessment of the interactions between the electron beam and the specimen is required. Estimating the crystal thickness beyond which dynamical diffraction is no longer negligible is not trivial, as there is no theoretically defined criterion. According to

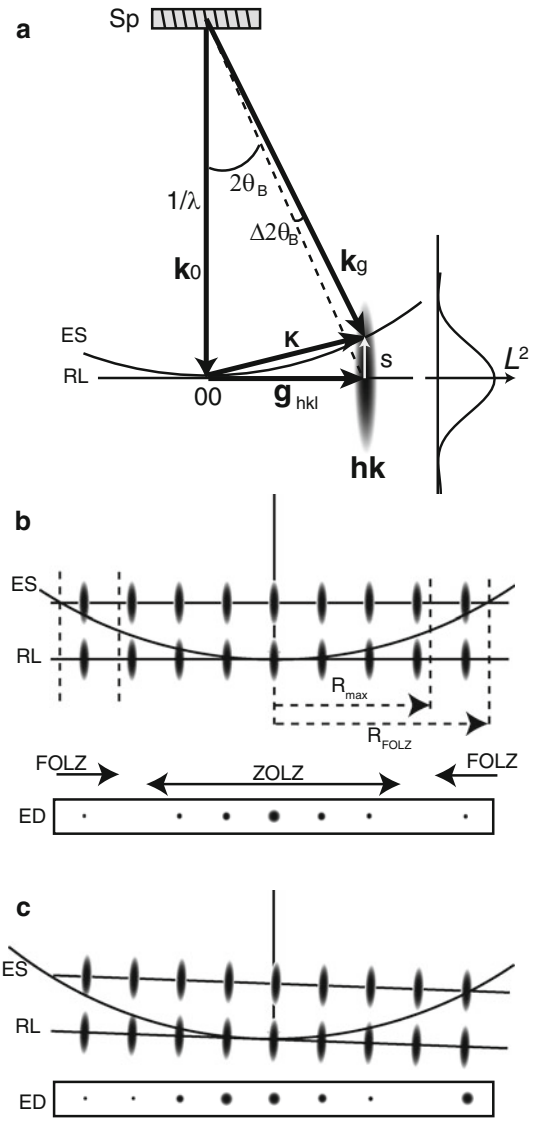

Fig. 1 **a** Schematic of the Ewald sphere (ES) and diffraction conditions for the investigated specimen (Sp). $\mathbf{k}_0$ and $\mathbf{k}_g$ represent the incident and diffracted wave vectors, RL designates a reciprocal lattice plane with one reciprocal *hk* node. The elongated reciprocal node intersects the ES out of perfect Bragg conditions ($2\theta_B + \Delta 2\theta_B$ angle) owing to the ES curvature (of $1/\lambda$ radius, λ being the electron wavelength). The excitation error vector ***s*** is the difference between the resulting diffraction vector **K** and the RL vector $\mathbf{g}_{hkl}$ for a given specimen orientation. The bell-shaped profile of the interference function L^2 is shown. **b** Intersection of the ES with reciprocal nodes of the RL showing a decrease in intensity of the RL nodes away from the RL origin. Reflections from the zero- and first-order Laue zones (ZOLZ and FOLZ) are shown. R_{FOLZ} and R_{max} indicate the mean radius of the FOLZ ring and the maximum radius of the ZOLZ beyond which both zones overlap. **c** Loss of ED centro-symmetry appears due to crystal misorientation

Cowley (1992), the kinematical approximation is valid only when the intensity of the direct beam overwhelms that of diffracted beams, thus precluding the use of the kinematical approximation for perfect single crystals. This strong requirement may, however, be softened for

imperfect crystals. For a mosaic crystal for example, Vainshtein (1956) and Drits (1987) defined the limit between kinematical and dynamical scattering as the crystal thickness leading to equal intensities for direct and diffracted beams. Based on the theory for the two-beam diffraction, the intensity ratio between diffracted and incident beams for mosaic crystals consisting of slightly disoriented blocks is:

$$I_{rel} = \frac{I_{\text{int}}}{I_0.S} = \frac{\lambda^2.F_{hkl}^2.t^2}{V_{cell}^2} \quad (1)$$

where I_{int} is the integrated intensity scattered by the mosaic crystal of thickness t, $I_0.S$ being the electron flux passing through the crystal. The thickness limit for the kinematical approximation to be valid ($I_{rel} < 1$), called critical thickness T_c, corresponds to (Vainshtein 1956; Drits 1987):

$$T_c < \frac{V_{cell}}{\lambda.F_{hkl}} \quad (2)$$

T_c depends on the *hkl* beam considered, but also on the unit-cell volume V_{cell}, on crystal chemistry and structure (atomic positions and site occupancy through F_{hkl}) and on the acceleration voltage (through both the electron wavelength λ and the elemental scattering factors corrected for relativistic effects—IUCr 1992). Various mineral structures have been solved for the first time using SAED techniques without taking dynamical effects into account (Drits 1987 and references therein). For example, the biopyribole three-chain structure was first determined using SAED and the kinematical approximation (Drits et al. 1975; Drits 1987).

Dynamical diffraction

If multiple scattering is not negligible, the intensity of a given diffracted beam is not simply related to its structure factor modulated by the shape factor. Rather, electron waves interact while traveling through the crystal leading to a transfer of intensity between diffracted and transmitted beams. Comparison with theoretical calculations is then required for the interpretation of intensity distribution. The Blockwaves (BW) method solves a system of Schrödinger equations describing the motion of electrons in the crystal for every beam transmitted or diffracted by the specimen. The Multislices (MS) approach, preferentially used in the present study, first divides the crystal in slices normal to the electron beam (Cowley and Moodie 1957; Humphreys and Bithell 1992). It then assumes (1) that the electron scattering from a given slice occurs in a single plane normal to the electron beam (projected potential plane) and is described by a phase-grating term and (2) that the transfer of the electron waves to the next plane is described by a propagation term through a uniform medium. As scattering and transfer normally occur simultaneously, the electron propagation through the crystal is best described when the slice thickness is minimum, artefacts potentially arising when the chosen slice is too thick.

Materials and methods

Samples

Two dioctahedral mica samples were chosen. The first one is an illite from the Athabasca basin, Canada, containing both tv-1*M* and cv-1*M* crystals of chemical formula $K^+_{1.6}{}^{[6]}\left(Al^{3+}_{3.7}Mg^{2+}_{0.2}Fe^{3+}_{0.1}\right)\,{}^{[4]}\left(Si^{4+}_{6.6}Al^{3+}_{1.4}\right)O_{20}(OH)_4$ (#8960-15, [1–2] μm fraction—Laverret et al. 2006). The second one is essentially a $2M_1$ illite from Kombolgie, Australia, of chemical composition $K^+_{1.75}{}^{[6]}\left(Al^{3+}_{3.85}Mg^{2+}_{0.05}Fe^{3+}_{0.10}\right)\,{}^{[4]}\left(Si^{4+}_{6.3}Al^{3+}_{1.7}\right)O_{20}(OH)_4$ (Patrier et al. 2003). No unambiguously identified 3*T* illite or muscovite was available, and this polytype could not be studied experimentally. Thickness of illite particles, as determined by atomic force microscopy scatters within the 80–250 Å range, with an average of ~150 Å. This value is consistent with the average number of TOT layers in coherent scattering domains determined from XRD profile modeling of *hkl* reflections (10–15 layers—Blin 2007), the proportion of random stacking faults being limited to 5%.

Transmission electron microscopy

Both mica powders were ultrasonically dispersed in de-ionized water and deposited onto Cu-mesh grids coated with holey carbon membranes. Samples were observed with a Philips 420 transmission electron microscope (TEM) equipped with a W filament operated at 120 kV. Additional observations were performed with a JEOL 2000*fx* LaB_6 TEM operated at 200 kV, a Philips/FEI CM300-FEG TEM (300 kV), and with a Hitachi H9000 NAR TEM (LaB_6, 300 kV) equipped with a Gatan Multiscan charge-coupled device (CCD) camera. Double-tilt sample holders were systematically used to orientate the crystals along their [001] zone axis. ED patterns were recorded for a large number of isolated single crystals, most of them with a reasonably low thickness (as estimated by the much higher intensity of the direct beam compared to diffracted ones), and flat surfaces (as estimated from the scarcity of bending contours in the image). SAED patterns were exposed on films using parallel-beam conditions (with illuminated area limited to 200 nm in diameter), a few being recorded on the CCD camera.

Electron diffraction calculation parameters

ED were calculated along the [001] direction for crystal thickness ranging from 0 to 400 Å using 50 Å steps. The acceleration voltage was set to 120 or 300 kV, and parallel

illumination conditions of SAED were mimicked by setting the half-convergence angle of the incident beam to 0.5 mrad. Reflections were calculated only for the ZOLZ.

Kinematical calculations were performed using the JEMS package (written by Stadelmann[1]). Acceleration voltage only acts as a scaling factor similar to the camera length. The deviation parameter (corresponding to the maximum excitation error *s* allowed, that is, to half the length of RL rods) was set to 0.2 nm^{-1} allowing the calculation of a sufficient number of diffraction beams and the systematic exclusion of first-order Laue zone (FOLZ) reflections.

Dynamical calculations were mainly performed with the MS method implemented in the MacTempas package (written by Kilaas[2]). The low half-convergence angle has no effect on the calculated intensities, but defines the diameter of the displayed diffraction spots for which a Gaussian intensity distribution is used. The "MS aperture" G_{max} parameter (related to the maximum excitation error *s* allowed) defines how far out in the reciprocal space the calculation extends and thus the number of electron beams included in the calculation. The 2 $Å^{-1}$ values used for G_{max} ensured that all significant contributions to the dynamical scattering were included. Indeed, the intensity summed over all transmitted and diffracted beams included in a 2 $Å^{-1}$ MS aperture shows no significant loss after iterations corresponding to a crystal thickness of 1,000 Å (<0.5% for cv-1*M*, < 0.1% for $2M_1$ and 3*T* polytypes at 300 kV—Fig. 2). The number of slices for the propagation term was systematically set to 6. For the potential term, the unit cells were not sub-sliced for the 1*M* and $2M_1$ polytypes, as observations were performed along the **c**-axis rather than along the normal to the layer **ab**-plane. For the sake of consistency, sub-slicing was not performed either for the 3*T* polytype, despite its larger unit-cell dimension ($c \sim 30$ Å). Though aluminous dioctahedral mica contain essentially $Z < 15$ elements, the absence of calculation artifacts was checked with calculations performed using the BW method available in the JEMS software (parameters set as for the kinematical case).

Structural models

A general structural formula of K-bearing 2:1 aluminous mica, which are the most abundant dioctahedral mica, is $K^{+}_{x+y}{}^{[6]}\left(Al^{3+}_{2-y}R^{2+}_{y}\right)^{[4]}\left(Si^{4+}_{4-x}Al^{3+}_{x}\right)O_{10}(OH)_2$ (Bailey 1984), where R^{2+} represents divalent cations (most commonly Mg^{2+} or Fe^{2+}). As Mg^{2+}, Al^{3+}, and Si^{4+} have similar scattering power, and because samples chosen for this study are Fe-poor, structural models for the ED calculations were based on the following "ideal" chemical formula of true mica $K^{[6]}Al_2{}^{[4]}Si_4O_{12}$. Four commonly reported polytypes and polymorphs were considered. Structure models for tv- and cv-1*M* illite polymorphs were taken from Drits et al. (1984a), while structure models for tv-$2M_1$ and tv-3*T* muscovite polytypes were retrieved from the ICSD database (#86622 and #75952—Amisano-Canesi et al. 1994; Liang et al. 1998). These polytypes crystallize in different space groups (Table 1). In particular, cv-1*M* and tv-3*T* structures differ from tv-1*M*, and tv-$2M_1$ ones by their non-centro-symmetrical character.

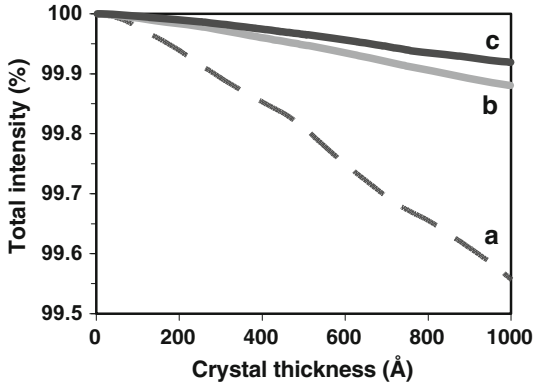

Fig. 2 Evolution of the total beam intensity transmitted through a $G_{max} = 2$ $Å^{-1}$ MS aperture for a 300 kV acceleration voltage. **a** cv-1*M* polytype; **b** $2M_1$ polytype; **c** 3*T* polytype

Table 1 Structure and symmetry parameters for tv-1*M*, cv-1*M*, tv-$2M_1$, and tv-3*T* polytypes of K-bearing dioctahedral mica

Polytype	TOT[a]	a[b]	b[b]	c[b]	β[b]	γ[b]	V_{cell}[b]	Space group
tv-1*M*	1	5.199	9.005	10.640	99.00	90	492.00	*C*2/*m*
cv-1*M*	1	5.199	9.005	11.064	101.30	90	507.94	*Cm*
tv-$2M_1$	2	5.177	8.987	20.007	95.76	90	929.09	*C*2/*c*
tv-3*T*	3	5.212	5.212	29.804	90	120	701.16	$P3_112$

[a] Number of TOT layers in the unit cell

[b] Unit-cell parameters in Å, angles in °; cell volume in $Å^3$

Results

Experimental SAED

When observed in the TEM, individual mica crystals are preferentially oriented normal to the **ab**-plane and need to be tilted to reach the [001] orientation. Along that zone axis, SAED patterns exhibit the same geometry but contrasted distributions of intensity between the ZOLZ reflections. For flat and isolated crystals, three groups of SAED patterns may be distinguished from their intensity distribution

[1] Electron Microscopy Suite, Java version (JEMS). http://cimewww.epfl.ch/people/stadelmann/jemswebsite/jems.html.

[2] MacTempas package from Total Resolution LLC. http://www.totalresolution.com/.

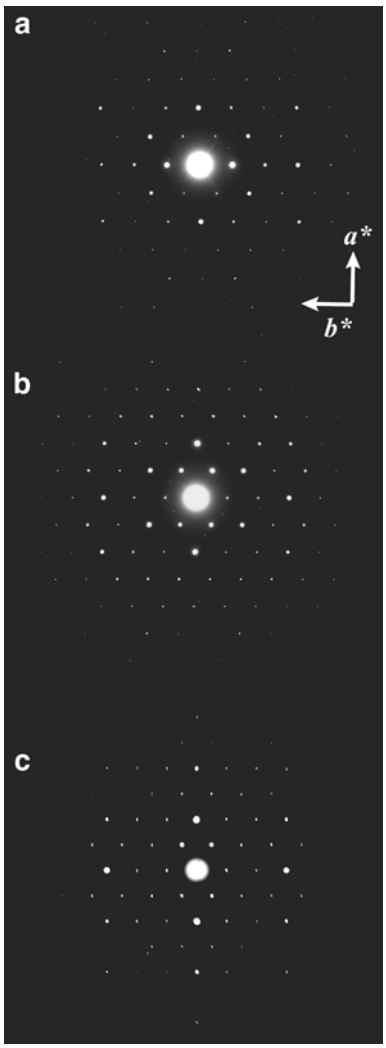

Fig. 3 Experimental SAED patterns of illite/muscovite crystals oriented along [001]. **a** type I (120 kV); **b** type II (200 kV); **c** type III (300 kV). Similar patterns were obtained for other voltages

(Fig. 3). Types I and II were mainly observed in the Athabasca sample (tv- and cv-1*M* polymorphs from XRD), while type III was recorded primarily in the Kombolgie sample ($2M_1$ polytype from XRD), together with type I patterns. As intensity distribution is likely controlled by crystal structure and/or thickness, theoretical ED patterns were calculated to assess the relative influence of these parameters, and possibly to define criteria of identification.

Calculated electron diffraction patterns: kinematical approximation

ED pattern indexing

A first series of kinematical calculations was performed ignoring crystal thickness and thus considering the sole effect of the structure factor. [001] ED patterns of tv-1*M*,

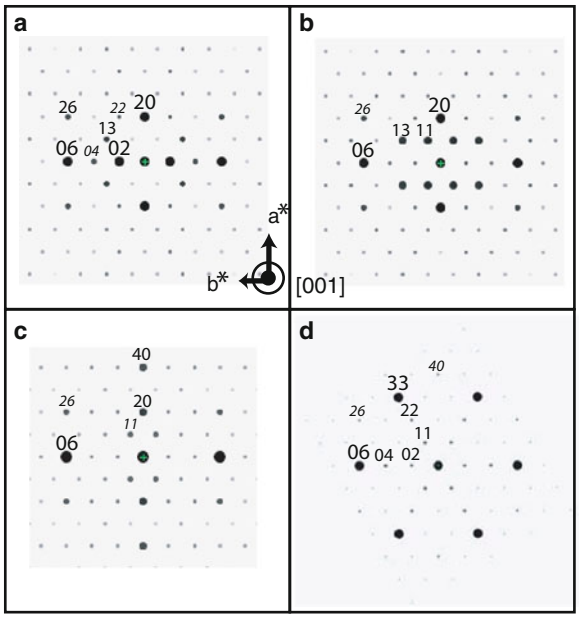

Fig. 4 ED patterns calculated along the [001] zone axis of different mica polytypes using the kinematical approximation. **a** tv-1*M*; **b** cv-1*M*; **c** $2M_1$; **d** 3*T*. Crystal thickness is not taken into account in the calculations. To ease the qualitative comparison with experimental diffraction patterns, diffraction intensities are proportional to the *gray scale* for the weaker spots and to the spot diameter for the most intense ones

cv-1*M*, tv-$2M_1$, and tv-3*T* polytypes display the same (pseudo-) hexagonal set of *hk*0 reflections (Fig. 4). As $\beta > 90°$ for 1*M* and $2M_1$ polytypes, [001] ED patterns were systematically indexed using an orthogonal **a*b*** unit cell with $a^* > b^*$ and $\gamma^* = 90°$. This 2D reciprocal cell is *C*-centered, and *hk*0 spots with $h + k \neq 2n$ (n integer) are extinct. The *l* index, null for ZOLZ reflections, will be omitted hereafter.

Structure factor effect

All four ED patterns present the same mirror planes normal to the **a***- and **b***-axes, but intensity distributions differ from one polytype or polymorph to the other (Fig. 4). For each structural variant, bright reflections can be grouped in three or four sets (Table 2), all other non-extinct reflections being very weak. The tv-1*M* ED pattern (Fig. 4a) contains three sets of intense *hk* reflections [(02, 20, 06), (13, 26), and (22, 04) and equivalent $\overset{\pm}{h}\,\overset{\pm}{k}$ reflections], while four sets can be defined for the cv-1*M* polytype [(20, 06), (11, 13), (26), and (02, 22)—Fig. 4b]. It follows that $\overset{\pm}{1}\,\overset{\pm}{1}$ reflections, more intense than $0\,\overset{\pm}{2}$ for the *cis*-vacant polymorph, could potentially be useful for the cv- *vs* tv-1*M* polymorph differentiation. The tv-$2M_1$ ED pattern (Fig. 4c) contains three other sets of intense reflections [(06), then (20, 40), and (11, 26)]. Finally, **c**- and **c***-axes being parallel for the tv-3*T* polytype, its [001] ED pattern (Fig. 4d) is strictly

Table 2 Indices of the brightest *hk* ($l = 0$) diffraction spots for tv-1*M*, cv-1*M*, tv-2M_1, and tv-3*T* polytypes of K-bearing aluminous dioctahedral mica

	tv-1*M*	cv-1*M*	tv-2M_1	tv-3*T*
1st set	(02), (20), (06)	(20), (06)	(06)	(06), (33)
2nd set	(13), (26)	(11), (13)	(20), (40)	(22), (04)
3rd set	(22), (04)	(26)	(11), (26)	(11), (02)
4th set		(02), (22)		(26), (40)

hexagonal and possesses a sixfold rotational symmetry, with very strong (06, 33) reflections of iso-intensity and weaker 22, 04, 11, and 02 (and equivalent) reflections.

Shape factor effect

For thin defect-free crystals, the beams far away from the ED pattern center are strongly excited owing to the elongation of the RL nodes, and the intensity distribution is similar to that described earlier. When crystal thickness increases, the elongation of RL nodes is reduced, thus reducing the intensity of *hk* spots when increasing their distance to the ED pattern center (Fig. 1b). This effect is illustrated for the 1*M* polymorphs (Figs. 5a–e, 6a–e) and for the other polytypes (Figs. 7a–e, 8a–e). For all structural variants, the characteristic intensity distribution is lost only for crystal thicker than ~300 Å.

Possible qualitative identification criteria

For each given crystal structure, kinematical [001] ED patterns thus possess specific sets of bright spots (Table 2; Fig. 4), whose indices essentially remain the same whatever the thickness, at least up to 200 Å. These intensity contrasts show unambiguously the impact of crystal structure on the intensity distribution between *hk*0 reflections and qualitative criteria based on these sets of *hk* indices may potentially be defined to identify the layer-stacking sequence (polytype) and the location of the octahedral vacancy (tv *vs* cv polymorphic variant).

Calculated electron diffraction patterns: dynamical approach

Before establishing qualitative identification criteria based on contrasted kinematical intensities, it is essential to check that dynamical effects induced by multiple scattering do not significantly modify diffracted beam intensities.

Thickness series for tv-1M

Figures 5f–j show the evolution of the dynamical ED pattern as a function of the crystal thickness for the tv-1*M*

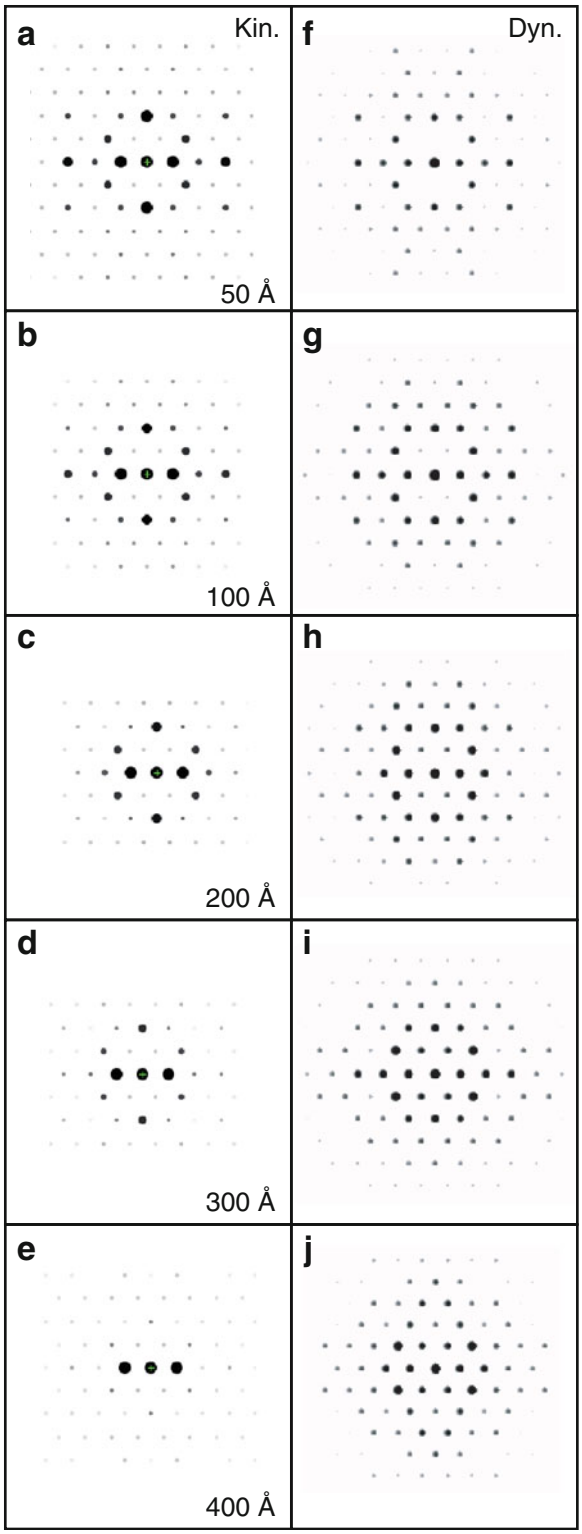

Fig. 5 ED patterns calculated along the [001] zone axis for tv-1*M* K-bearing aluminous mica. **a–e** Calculations performed with the kinematical approximation and taking into account the crystal thickness; **f–j** calculations performed with the dynamical diffraction theory (Multislices method) for a 300 kV acceleration voltage. Crystal thicknesses are indicated for the different ED patterns

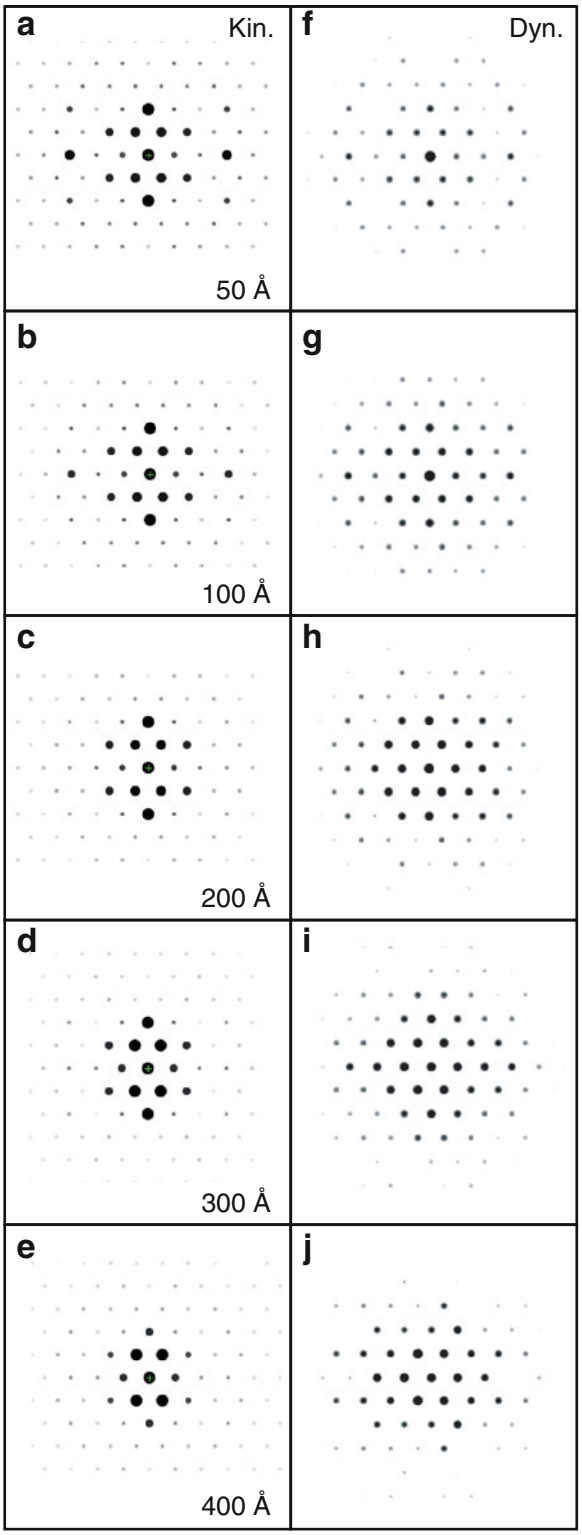

Fig. 6 ED patterns calculated along the [001] zone axis for cv-1*M* dioctahedral K-bearing aluminous mica. **a–e** Kinematical case; **f–j** dynamical case (MS, 300 kV)

model. For a 50 Å thickness and a 300-kV electron beam (Fig. 5f), the intensity distribution is similar to the kinematical case. But with thickness increase, the intensity gets concentrated and homogenized among the *hk* reflections directly around the central beam. In addition, the intensity of a given reflection shows complex evolution (for ex. 06 reflections first fades before regaining in brightness in the 300–400 Å range). As a result, the calculated ED patterns of thick crystals no longer present characteristic features allowing the identification of this structure.

Fig. 7 Pendellosung plots of the intensity calculated for specific *hk0* beams (dynamical MS method). Beam intensities are given as a percentage of the total beam intensity. **a** tv-1*M* polytype: 020/0$\bar{2}$0 beams at 120 and 300 kV (*bold* and *light solid lines*, respectively) and 110/1$\bar{1}$0 beams at 120 and 300 kV (*bold* and *light dashed lines*, respectively); **b** cv-1*M* polytype at 300 kV: 110 and 1$\bar{1}$0 beams (*bold dashed* and *solid lines*, respectively), 020 and 0$\bar{2}$0 beams (*light dashed* and *solid lines*, respectively); **c** cv-1*M* polytype at 120 kV: patterns as Fig. 7b. **d** 000 beam for the tv-1*M* polytype at 120 and 300 kV (*light solid* and *dashed lines*, respectively), and for the cv-1*M* polytype at 120 kV (*bold solid line*)

Thickness series for cv-1M

Major modifications of the intensity distribution are also observed for the cv polymorph when increasing the crystal thickness (Figs. 6f–j). In particular, the intensity contrast between 11 and 02 reflection sets, which potentially allows differentiating cv- and tv-1*M* mica, is weakened when taking dynamical effects into account. Pendellosung plots (Cowley 1992; Ewald 1917) allow a better visualization of the predicted intensity evolution as a function of crystal thickness resulting from complex beam interactions. In contrast to the tv-1*M*, for which 020 beams remain brighter than 110 ones whatever the crystal thickness (Fig. 7a), the 110/020 intensity ratio can even get reversed for cv crystals thicker than 250–280 Å (Fig. 7b). More important, the mirror plane perpendicular to the **b***-axis is lost thus violating the Friedel centro-symmetry law of the diffraction pattern. From a 50 Å thickness and up, the intensity of the 110/1$\bar{1}$0 beams and 020/0$\bar{2}$0 beams differ indeed, the oscillations of their intensity curves being totally out of phase above 250–280 Å (Fig. 6b). For a lower incident beam energy dynamical effects are enhanced due to stronger interactions, and out-of-phase oscillations are visible for thinner crystals (205 Å for 120 kV, Fig. 7c and Online Resource 1). For 400 Å, the ED pattern gets totally acentric (Fig. 6j), and the 11 and $\bar{1}$1 spots become more intense than the central beam, which becomes difficult to identify. Plot of the 000 beam intensity shows that the strong interaction at 120 kV weakens the 000 beam from 20 to 5% only of the total intensity for thickness between 250 and 400 Å, while the 110 and $\bar{1}$10 beams account for 12–22% of the total intensity over the same crystal thickness range (Fig. 7c–d). Similar results were obtained with the BW method (not shown).

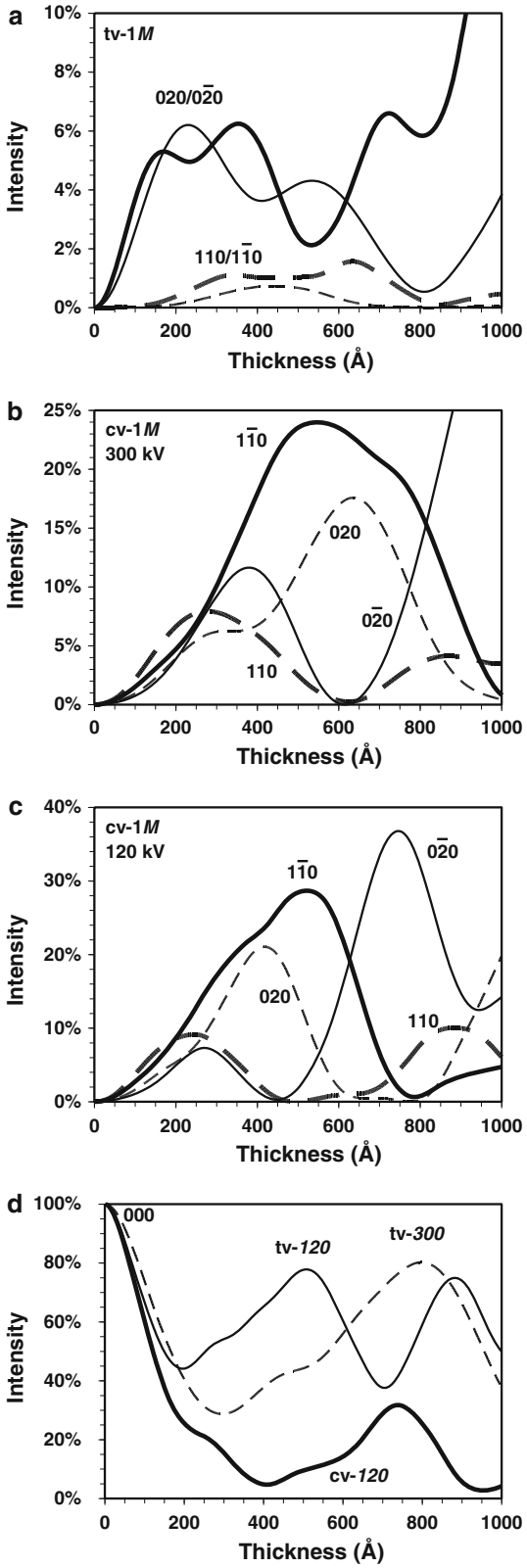

Thickness series for tv-2M_1 and tv-3T

As for 1*M* polytypes, the ED pattern of the $2M_1$ polytype calculated for 50-Å-thick crystals (Fig. 8f) is similar to the kinematical calculation, the characteristic set of bright spots being lost for 200-Å-thick crystals (10 unit cells—Fig. 8h). For the 3*T* polytype, a close look at the pattern

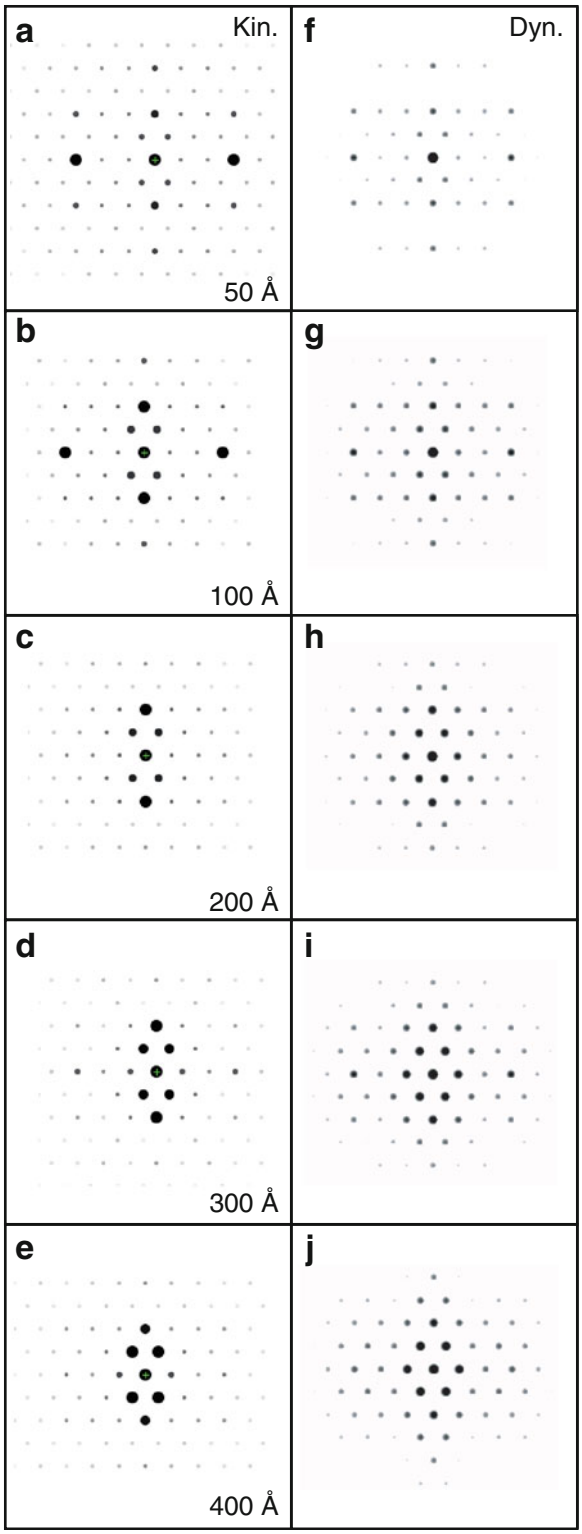

Fig. 8 ED patterns calculated along the [001] zone axis for $2M_1$ dioctahedral K-bearing aluminous mica. **a–e** Kinematical case; **f–j** dynamical case (MS, 300 kV)

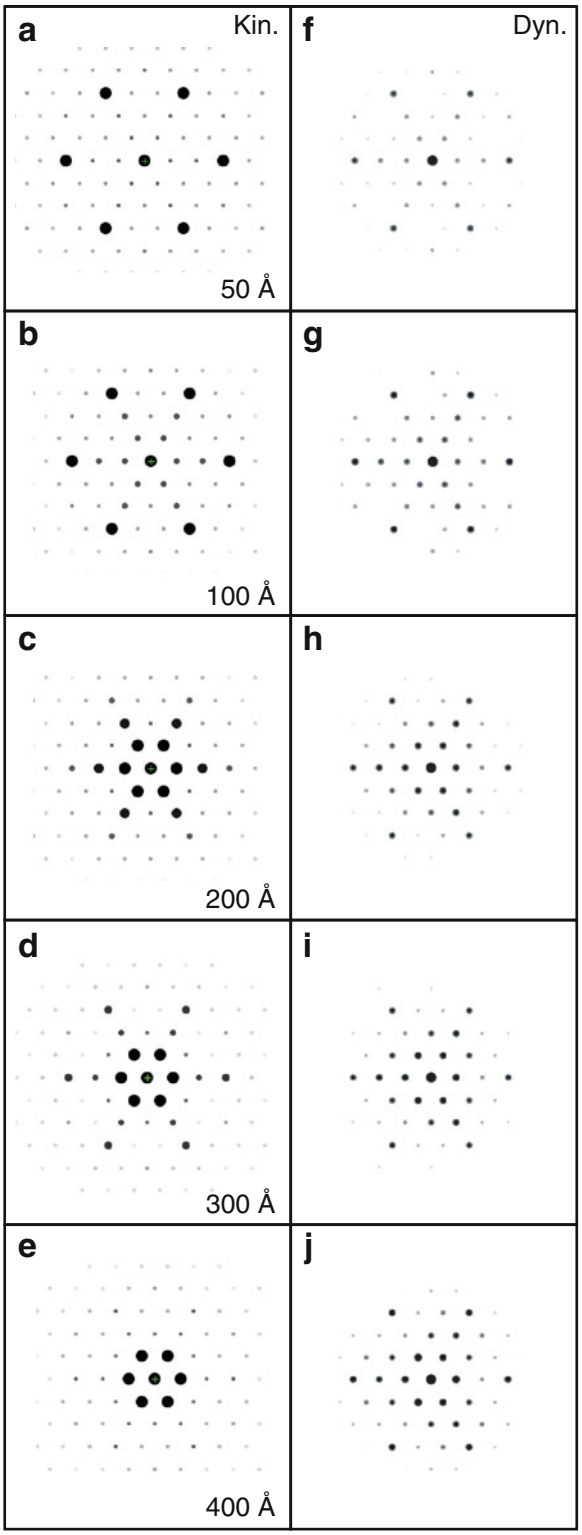

Fig. 9 ED patterns calculated along the [001] zone axis for 3*T* dioctahedral K-bearing aluminous mica. **a–e** Kinematical case; **f–j** dynamical case (MS, 300 kV)

calculated for 50-Å-thick crystals (Fig. 9g) reveals that its sixfold rotational symmetry is not perfectly respected. Instead, patterns calculated for 100-Å-thick crystals clearly present a threefold rotational axis (Fig. 9g–j). Additional calculations performed using the BW method are fully consistent with the MS results, demonstrating that the loss of center of symmetry is not due to non-sub-slicing of the projected potential (see Online Resource 2).

Overall dynamical effects

For all polytypes and polymorphs, strong dynamical effects are predicted for crystals thicker than 100 Å or less. Though detailed effects are specific to each structure, three main features are systematically observed when increasing crystal thickness. First, there is a strong redistribution of the intensity between direct and diffracted beams that tends to homogenize the intensity over the whole diffraction pattern. Second, the intensity of diffracted beams is not affected evenly by a crystal thickness increase, and the set of bright spots specific to each polytype and polymorph vanishes with increasing thickness. Third, there is an apparent violation of the Friedel law $I(hk) = I(\bar{h}\bar{k})$ in the case of cv-1*M* and tv-3*T* polytypes whose unit cells are not centro-symmetrical.

Discussion

Consistent with experimental data, ED patterns calculated for dioctahedral mica along [001] differ by their intensity distribution despite a similar geometry. But important dynamical effects are predicted, which may impair the usefulness of SAED for dioctahedral aluminous mica polytype and polymorph identification. Therefore, experimental and calculated ED patterns are compared below and the origin of some discrepancies is discussed. Impact of high proportion of defects as well as some experimental settings during data acquisition is also addressed.

Comparison of experimental and calculated SAED patterns

To our knowledge, no systematic comparison of experimental SAED patterns with calculations based on both kinematical and dynamical diffraction theories was ever published for mica. But though dynamical theory should be preferred for interpretation of SAED intensity distribution, it is, however, relevant to check whether such calculations are really essential because of their intrinsic complexity.

Experimental versus kinematical ED patterns

SAED patterns of type I, II and III (Fig. 3) match those calculated for tv-1*M*, cv-1*M*, and tv-2M_1 dioctahedral

Table 3 Critical thickness T_c for tv-1*M*, cv-1*M*, tv-2M_1, and tv-3*T* polytypes of K-bearing dioctahedral mica calculated from Eq. 2

Strongest *hkl*	tv-1*M* 020	cv-1*M* 060	tv-2M_1 33$\bar{1}$/060	tv-3*T* 060/330
80 kV			316 Å*/321 Å	
120 kV	224 Å	372 Å	369 Å/376 Å	473 Å
300 kV	397 Å	492 Å	488 Å/497 Å	626 Å

* Güven (1974b) calculated a 363 Å T_c value for the strongest 33$\bar{1}$ beam of the 2M_1 muscovite polytype and a 80-kV microscope. Difference may arise from minor differences in the structure parameters

mica, respectively, using the kinematical approximation without specimen thickness consideration (Fig. 4a–c). This qualitative agreement is achieved whatever the electron source coherence (W, LaB_6, FEG) and the acceleration voltage (120–300 kV—data not shown). One can note that if thickness is taken into account, experimental 06 and 26 beams are systematically brighter than calculated, indicating additional RL node elongation likely due to the imperfect crystal structure. Overall, it is, however, possible to define for each given polytype and polymorph characteristic sets of strong reflections (Table 2) that may be used for its identification. Note that since we did not possess clearly identified 3*T* illite or muscovite sample, agreement could not be checked for this polytype. No SAED pattern corresponding to this structure was observed in the samples analyzed during this work.

Comparison with dynamical ED patterns

In contrast to the kinematical case, ED patterns calculated with the dynamical theory do not compare well with experimental data (except for crystal thickness below 100 Å, that is < 10 TOT layers). Even for the lowest acceleration voltage used (120 kV), for which probability of multiple scattering is the highest, dynamical diffraction effects, such as the loss of characteristic bright spot patterns or the loss of centro-symmetry for the cv-1*M* polytype, were not observed. It was not possible either to evidence non-centro-symmetry when recording SAED patterns on a CCD camera (data not shown), the faint intensity difference measured between *hk*0 and $\bar{h}\bar{k}$0 spots in this case being clearly due to a slight misorientation of the crystal.

Validity of kinematical approximation

Illite crystals are composed mainly of lights atoms (O, Si, Al, Mg) and have large unit-cell dimensions [$\sim$5.2 $\times$ 9.0 $\times$ (n $\times$ 10.0) Å^3]. These properties favor kinematical diffraction as shown by the high values of critical thickness T_c (Table 3), the lowest being 224 Å for the tv-1*M* polytype at 120 kV, which is greater than the average value of $\sim$150 Å for the thickness of illite crystals. This last value is also in good agreement with the mean number of TOT layers deduced from XRD profile analysis (coherent scattering domains, CSDs, of 10–15 layers). These results are likely responsible for the good match between calculated kinematical ED patterns and the data. In addition, the systematic occurrence of similar *hkl* intensity distributions for various crystals of the same mineral commonly described by a log-normal distribution of CSDs, as experimentally observed in this study, further support the absence or weakness of the dynamical effects.

Non-observation of predicted dynamical effects

Despite the agreement between experimental ED patterns and kinematical calculations, the thickness limit for calculated dynamical effects is far smaller (as low as 50 Å with a loss of center of symmetry for cv-1*M*—Figs. 6f, g and 7b, c) than the T_c values estimated from Eq. 2. The latter values set an absolute maximum for mosaic crystals, which is smoothing some of the dynamical effects, but not an exact boundary. This apparent contradiction indicates that at least one important parameter is omitted in the calculations. One can first note that the experimental I_{hkl}/I_{000} intensity ratio for any diffracted beam (Fig. 3) appears lower than predicted by the calculations, thus suggesting an overestimation of the scattering probability. This discrepancy is likely a key to the non-observation of predicted dynamical effects. Calculations are indeed based on a diffraction theory developed for perfect crystals, while natural mica contains significant proportions of structural defects. Cowley (1992) pointed out that "it is necessary to know how the intensities may be modified if the crystal thickness or degree of lattice perfection is such that some "dynamical" scattering takes place". In contrast, a variety of structural defects in natural mica likely precludes dynamical scattering.

First, 1*M* and 2M_1 illite samples normally contain 3–10% of expandable layers (Drits et al. 2010). Even under vacuum, smectite interlayers disturb the 3D coherence by inducing translational/rotational defects of parallel layers (Guthrie and Reynolds 1998). Random stacking faults, which are common in layered structures such as mica, also reduce the size of CSDs, although the simulation of XRD line profiles indicates that the occurrence probability of random stacking faults is limited to $\sim$5% in our 1*M* mica samples (Blin 2007). The resulting thin CSDs induce a further elongation of RL nodes. Intensity recorded for reflections far from the ED pattern center (e.g. 060) is also likely reinforced by the small spread of the incident beam. A given diffracted beam results, however, from the sum of electron waves scattered by each atom of the specimen. So, for a crystal out of perfect Bragg orientation, these waves

are out of phase and their mutual annihilation through destructive interferences prevents the building of strong diffracted beams compared to defect-free crystals (Drits 1987). The likelihood and impact of multiple scattering are thus severely reduced, accounting logically for the discrepancy between calculated dynamical intensity distributions and the data.

Second, Kodama et al. (1971) showed from the analysis of the XRD 00*l* reflection profiles that microcrystalline muscovite lattice was distorted along **c***-axis and attributed this distortion to non-uniform basal distances linked to an irregular distribution of interlayer cations. Indeed, 1*M* and $2M_1$ illites are commonly K-deficient compared to the ideal mica structure (Kodama et al. 1971; Meunier and Velde 1989; Lanson and Champion 1991; Srodon et al. 1992). Such distortion of the direct lattice also results in an elongation of the RL rods and a smoothing of dynamical effects. The possible interstratification of polytypic fragments further increases the elongation of RL rods along **c***-direction. However, this type of stacking defects also modifies *F*(*hkl*) values, thus bringing additional complexity to SAED patterns and hampering their interpretation.

Finally, the lateral sizes of illite particles are much longer than those of the CSDs in the **ab-**plane owing to crystal mosaicity. This additional partial disorientation of CSDs forming illite particles further decreases the occurrence of dynamical effects.

To summarize, the non-observation of dynamical effects in experimental SAED patterns (though they may exist to some extent) most likely originates from the elongation of RL nodes that does not originate only from crystal thickness but may arise also from factors linked to the imperfect structure of natural mica crystals. This allows defining qualitative identification criteria based on the simple kinematical approach.

FOLZ extension and experimental settings

On a practical perspective, RL nodes elongation and their impact on ZOLZ reflections intensities can be estimated. In addition, experimental parameters such as the lens settings and the crystal orientation may also modify the diffracted intensity, and their influence should be taken into account as they can impair the use of identification criteria.

Table 4 Maximum extension R_{max} of the ZOLZ ensuring absence of FOLZ and ZOLZ overlapping and radius R_{FOLZ} of the FOLZ calculated from Eq. 3

	R_{max}/R_{FOLZ} (Å^{-1})		
	1*M*	$2M_1$	3*T*
120 kV	1.73/2.44	1.22/1.73	1.00/1.41
300 kV	2.25/3.19	1.59/2.25	1.30/1.84

RL elongation and FOLZ extension

Observation of SAED pattern is possible only due to elongation of RL nodes, which also favors kinematical diffraction. An excessive elongation of RL nodes may, however, lead to a feeding of the FOLZ reflections into the ZOLZ (Fig. 1b) altering *hk* spots intensities. Experimentally, a separate FOLZ reflections ring is often not visible, so absence of feeding needs then to be checked by another mean. Overlapping of the FOLZ and ZOLZ does not happen if the half-length of the elongated RL nodes remains lower than 1/2c. In absence of defects, this condition is fulfilled for two unit-cell thick crystals (ignoring secondary maxima of the shape function—Güven 1974b). Additional elongation due to a high proportion of defects may, however, lead to such problem. The radius corresponding to the intersection of the ES with the *hkl* RL plane (R_{FOLZ}) and that corresponding to the maximum extension of the ZOLZ (R_{max}) beyond which it overlaps with the FOLZ (Fig. 1b) can be estimated from the following equations:

$$R_{max} = \left(\frac{1}{\lambda.c} - \frac{1}{4c^2}\right)^{1/2} \text{ and } R_{FOLZ} = \left(\frac{2}{\lambda.c} - \frac{1}{c^2}\right)^{1/2}. \quad (3)$$

The smallest R_{max} value (Table 4), obtained for the 3*T* polytype and an energy of 120 kV, is far greater than d^*_{060} (1.00 vs. 0.69 Å^{-1}). Thus, although elongation of reciprocal nodes is observed experimentally, for example when tilting the specimen, the intensity of all spots with $h + k \leq 6$ arises only from the *hk*0 beams.

Lens settings

For HRTEM image calculations, the transfer function of the objective lens is applied to the exit waves to account for the phase modification. This final step is most often omitted for the ED pattern calculation, though the objective lens likely impacts the diffraction pattern occurring in its focal plane (Güven 1974b). However, on modern instruments, this parameter does not appear to have a significant effect on diffracted intensities unless the lens is totally out-of-focus. If care is taken to keep the image and the diffraction pattern in-focus before collecting SAED patterns, limited effect is expected from this parameter.

Crystal orientation

ED calculations reported in the present work were performed with a perfect orientation of the crystal along the [001] zone axis. Such perfection is, however, difficult to

achieve experimentally, thus inducing a slight modification of the intensity distribution (Fig. 1c). But if it remains limited, the polytype and polymorph identification may still be possible using the defined criteria, the main experimental challenge being to determine the [001] orientation.

Conclusions

Several ED techniques were developed over the past 50 years to solve crystal structures. OTED proved to be a very efficient tool but has been used only in the former USSR countries and is now essentially abandoned. CBED is appropriate for thick crystals and requires comparison with dynamical calculations. PED is more recent, and appears promising for electron crystallography as intensity distributions are little dependent on crystal thickness and experimental parameters. It will likely advantageously replace SAED, which remains at present the most widely used ED technique, although dynamical simulations are often necessary to interpret unambiguously diffracted intensity distributions. In many cases though, such as the one described in the present study, SAED provides structural information far beyond the sole geometrical information. For finely divided dioctahedral mica, occurrence of structural imperfections tends to reduce likelihood of multiple scattering. Dynamical calculations are thus not necessary to interpret, to a certain extent, experimental SAED intensity distributions in structural terms. However, as diffraction intensities depends on numerous parameters (thickness, orientation, nature and amount of disorder, wavelength, exact chemical composition, etc.), it is not possible to establish quantitative criteria. Nevertheless, providing a limited stacking disorder and absence of heavy element substitution, the widely available SAED technique can potentially be used to differentiate tv- from cv-1*M* polymorph, and other polytypes ($2M_1$ and 3*T*) by qualitative comparison of experimental [001] ED patterns with kinematical calculations. Additional recording of SAED patterns along other zone axes close to [001] can be useful to validate the identification.

Acknowledgments This work was supported by a NSF grant #EAR0409071 (ACG, and DRV) and a Lavoisier fellowship (French Ministry of Foreign Affairs) to ACG. VAD thanks the Russian Foundation for Basic Research for financial support. Daniel Beaufort (Hydr'Asa, Poitiers—France) and Roar Kilaas (Total Resolution, Berkeley—USA) are thanked for providing the mica samples and for valuable discussions about the MacTempas software, respectively. Alain Baronnet (CINaM, Marseille—France) and Ken Livi (JHU, Baltimore—USA) are thanked for providing TEM access, assistance, and for fruitful discussions. The present version of the article benefited from the constructive comments of three anonymous reviewers.

References

Amisano-Canesi A, Chiari G, Ferraris G, Ivaldi G, Soboleva SV (1994) Muscovite-3T and phengite-3T–Crystal-structure and conditions of formation. Eur J Mineral 6(4):489–496

Amouric M, Baronnet A (1983) Effect of early nucleation conditions on synthetic muscovite polytypism as seen by high-resolution transmission electron microscopy. Phys Chem Miner 9(3–4): 146–159

Amouric M, Baronnet A, Finck C (1978) Polytypisme et désordre dans les micas dioctaédriques synthétiques: étude par imagerie de réseau. Mater Res Bull 13(6):627–634

Amouric M, Mercuriot G, Baronnet A (1981) On computed and observed HRTEM images of perfect mica polytypes. B Mineral 104(2–3):298–313

Bailey SW (1984) Classification and structure of the micas. In: Bailey SW (ed) Micas. Mineralogical Society of America, Chelsea, vol 13, pp 1–12

Bailey SW (1988) Hydrous phyllosilicates (exclusive of micas), vol 19. Reviews in Mineralogy. Mineralogical Society of America, Chelsea

Beermann T, Brockamp O (2005) Structure and analysis of montmorillonite crystallites by convergent-beam electron diffraction. Clay Miner 40(1):1–13

Blin A (2007) Illites: liens entre morphologie et structure–Influence sur la thermodynamique de la nucléation et de la croissance. Dissertation, University of Poitiers, France

Cowley JM (1992) Electron diffraction techniques. In: IUo (ed) Crystallography. IUCr Monographs on crystallography, vol 3. Oxford University Press, Oxford

Cowley JM, Moodie AF (1957) Fourier images: I–The point source. Proc Physic Soc B70(5):486–496

Drits VA (1987) Electron diffraction and high-resolution electron microscopy of mineral structures. Spring, New-York

Drits VA, Sakharov BA (2004) Potential problems in the interpretation of powder X-ray diffraction patterns from fine-dispersed 2M1 and 3T dioctahedral micas. Eur J Mineral 16(1):99–110

Drits VA, Goncharov YI, Aleksandrova VA, Khadzhi VE, Dmitrik AL (1975) New type of strip silicate. Sov Phys Crystallogr 19:737–741 (translated from Kristallografiya, 1974, 19:1186–1193)

Drits VA, Plançon A, Sakharov BA, Besson G, Tsipursky SI, Tchoubar C (1984a) Diffraction effects calculated for structural models of K-saturated montmorillonite containing different types of defects. Clay Miner 19(4):541–562

Drits VA, Tsipursky SI, Plançon A (1984b) Application of the method for the calculation of intensity distribution to electron diffraction structural analysis. Izvestya Akademii Nauk SSSR, Seriya Physic 2:1708–1713 (in Russian)

Drits VA, Weber F, Salyn AL, Tsipursky SI (1993) X-ray identification of one-layer illite varieties: application to the study of illites around uranium deposits of Canada. Clays Clay Miner 41(3):389–398

Drits VA, Lindgreen H, Salyn AL, Ylagan RF, McCarty DK (1998) Semiquantitative determination of trans-vacant and cis-vacant 2:1 layers in illites and illite-smectites by thermal analysis and X-ray diffraction. Am Mineral 83(11–12 (1)):1188–1198

Drits VA, McCarty DK, Zviagina BB (2006) Crystal-chemical factors responsible for the distribution of octahedral cations over *trans*- and *cis*-sites in dioctahedral 2:1 layer silicates. Clays Clay Miner 54(2):131–152

Drits VA, Zviagina BB, McCarty DK, Salyn AL (2010) Factors responsible for crystal-chemical variations in the solid solutions from illite to aluminoceladonite and from glauconite to celadonite. Am Mineral 95(2–3):348–361

Durovic S (1992) Layer stacking in general polytypic structures. In: Wilson AJC (ed) International tables for crystallography–C Mathematical, physical and chemical tables, vol C. Kluwer Academic Publisher, Dordrecht, pp 667–680

Emmerich K, Kahr G (2001) The cis- and trans-vacant variety of a montmorillonite: an attempt to create a model smectite. Appl Clay Sci 20(3):119–127

Emmerich K, Madsen FT, Kahr G (1999) Dehydroxylation behavior of heat-treated and steam-treated homoionic cis-vacant montmorillonites. Clays Clay Miner 47(5):591–604

Ewald PP (1917) On the explanation of crystal optics. Annalen Der Physik 54(23):519–556

Gemmi M, Nicolopoulos S (2007) Structure solution with three-dimensional sets of precessed electron diffraction intensities. Ultramicroscopy 107:403–494

Guthrie GD, Reynolds RC (1998) A coherent TEM- and XRD-description of mixed-layer illite/smectite. Can Mineral 36(6): 1421–1434

Güven N (1974a) Electron-optical investigations on montmorillonites–I Cheto, Camp-Berteaux and Wyoming montmorillonites. Clays Clay Miner 22(2):155–165

Güven N (1974b) Factors affecting selected area electron diffraction patterns of micas. Clays Clay Miner 22(1):97–106

Humphreys CJ, Bithell EG (1992) Electron diffraction theory. In: Cowley JM (ed) Electron diffraction techniques, vol 3. Oxford University Press, Oxford, pp 75–151

IUCr (1992) International tables for crystallography-C. Mathematical, physical and chemical tables, vol C. International Tables for Crystallography. Kluwer Academic Publisher, Dordrecht

Kameda J, Miyawaki R, Drits VA, Kogure T (2007) Polytype and morphological analyses of Gümbelite, a fibrous Mg-rich illite. Clays Clay Miner 55(5):453–466

Kodama H, Gatineau L, Mering J (1971) Analysis of X-ray diffraction line profiles of microcrystalline muscovites. Clays Clay Miner 19(6):405–413

Kogure T (2002a) Identification of polytypic groups in hydrous phyllosilicates using electron backscattering patterns. Am Mineral 87(11–12):1678–1685

Kogure T (2002b) Investigation of micas using advanced transmission electron microscopy. In: Mottana A, Sassi FP, Thompson JB Jr, Guggenhein S (eds) Micas: crystal chemistry and metamorphic petrology, vol 46. Mineralogical Society of America, Washington, pp 281–310

Kogure T, Drits VA (2010) Structural change in celadonite and *cis*-vacant illite by electron radiation in TEM. Clays Clay Miner 58(4):522–531

Kogure T, Nespolo M (1999) First occurrence of a stacking sequence including (+60°, 180°) rotations in Mg-rich annite. Clays Clay Miner 47(6):784–792

Kogure T, Kameda J, Drits VA (2008) Stacking faults with 180° layer rotation in celadonite, an Fe- and Mg-rich dioctahedral mica. Clays Clay Miner 56(6):612–621

Lanson B, Champion D (1991) The I/S-to-illite reaction in the late stage diagenesis. Am J Sci 291(5):473–506

Lanson B, Beaufort D, Berger G, Baradat J, Lacharpagne J-C (1996) Illitization of diagenetic kaolinite-to-dickite conversion series: late-stage diagenesis of the Lower Permian Rotliegend Sandstone reservoir, offshore of the Netherlands. J Sediment Res 66(3):501–518

Lanson B, Beaufort D, Berger G, Bauer A, Cassagnabere A, Meunier A (2002) Authigenic kaolin and illitic minerals during burial diagenesis of sandstones: a review. Clay Miner 37(1):1–22

Laverret E, Patrier Mas P, Beaufort D, Kister P, Quirt D, Bruneton P, Clauer N (2006) Mineralogy and geochemistry of the host-rock alterations associated with the Shea Creek unconformity-type uranium deposits (Athabasca Basin, Saskatchewan, Canada). Part 1. Spatial variation of illite properties. Clays Clay Miner 54(2):275–294

Liang JJ, Hawthorne FC, Swainson IP (1998) Triclinic muscovite: X-ray diffraction, neutron diffraction and photo-acoustic FTIR spectroscopy. Can Mineral 36:1017–1027

Meunier A, Velde B (1989) Solid solutions in I/S mixed-layer minerals and illite. Am Mineral 74(9–10):1106–1112

Moeck P, Rouvimov S (2010) Precession electron diffraction and its advantages for structural fingerprinting in the transmission electron microscope. Zeit Krist 225:110–124

Nicolopoulos S, Morniroli J-P, Gemmi M (2007) From powder diffraction to structure resolution of nanocrystals by precession electron diffraction. Zeit Krist Suppl 26:183–188

Patrier P, Beaufort D, Laverret E, Bruneton P (2003) High-grade diagenetic dickite and 2 M(1) illite from the Middle Proterozoic Kombolgie formation (Northern Territory, Australia). Clays Clay Miner 51(1):102–116

Plançon A, Tsipursky SI, Drits VA (1985) Calculation of intensity distribution in the case of oblique texture electron diffraction. J Appl Crystallogr 18:191–196

Srodon J, Elsass F, McHardy WJ, Morgan DJ (1992) Chemistry of illite-smectite inferred from TEM measurements of fundamental particles. Clay Miner 27:137–158

Tsipursky SI, Drits VA (1977) Effectiveness of the electronic method of intensity measurement in structural investigation by electron diffraction. Izv An SSSR Fiz+ 1:2263–2271 (in Russian)

Vainshtein BK (1956) Structural electronography. (English translation) edn. Akademii Nauk SSSR, Moscow (English translation)

Weiss Z, Wiewiora A (1986) Polytypism of micas. III. X-ray diffraction identification. Clays Clay Miner 34(1):53–68

Zviagina BB, Sakharov BA, Drits VA (2007) X-ray diffraction criteria for the identification of trans- and cis-vacant varieties of dioctahedral micas. Clays Clay Miner 55(5):467–480

Zvyagin BB (1967) Electron diffraction analysis of clay mineral structures (Elektronografiya i strukturanaya kristallografiya glinistykh mineralov (1964)). Plenum, New York

Zvyagin BB, Vrublevskaya ZV, Zhoukhlistov AP, Sidorenko OV, Soboleva SV, Fedotov AF (1979) High-voltage electron diffraction in the study of layer minerals. Nauka Press, Moscow

Supplemental information for the paper (in *Physics and Chemistry of Minerals*)

"Polymorph and polytype identification of finely divided aluminous dioctahedral mica individual crystals with SAED. Kinematical and dynamical electron diffraction."

Anne-Claire Gaillot, Victor A. Drits, David R. Veblen, Bruno Lanson

Institut des Matériaux Jean Rouxel (IMN), Université de Nantes, CNRS, 2 rue de la Houssinière, BP 32229, 44322 Nantes Cedex 3, France - Anne-Claire.Gaillot@cnrs-imn.fr

Online Resource 1

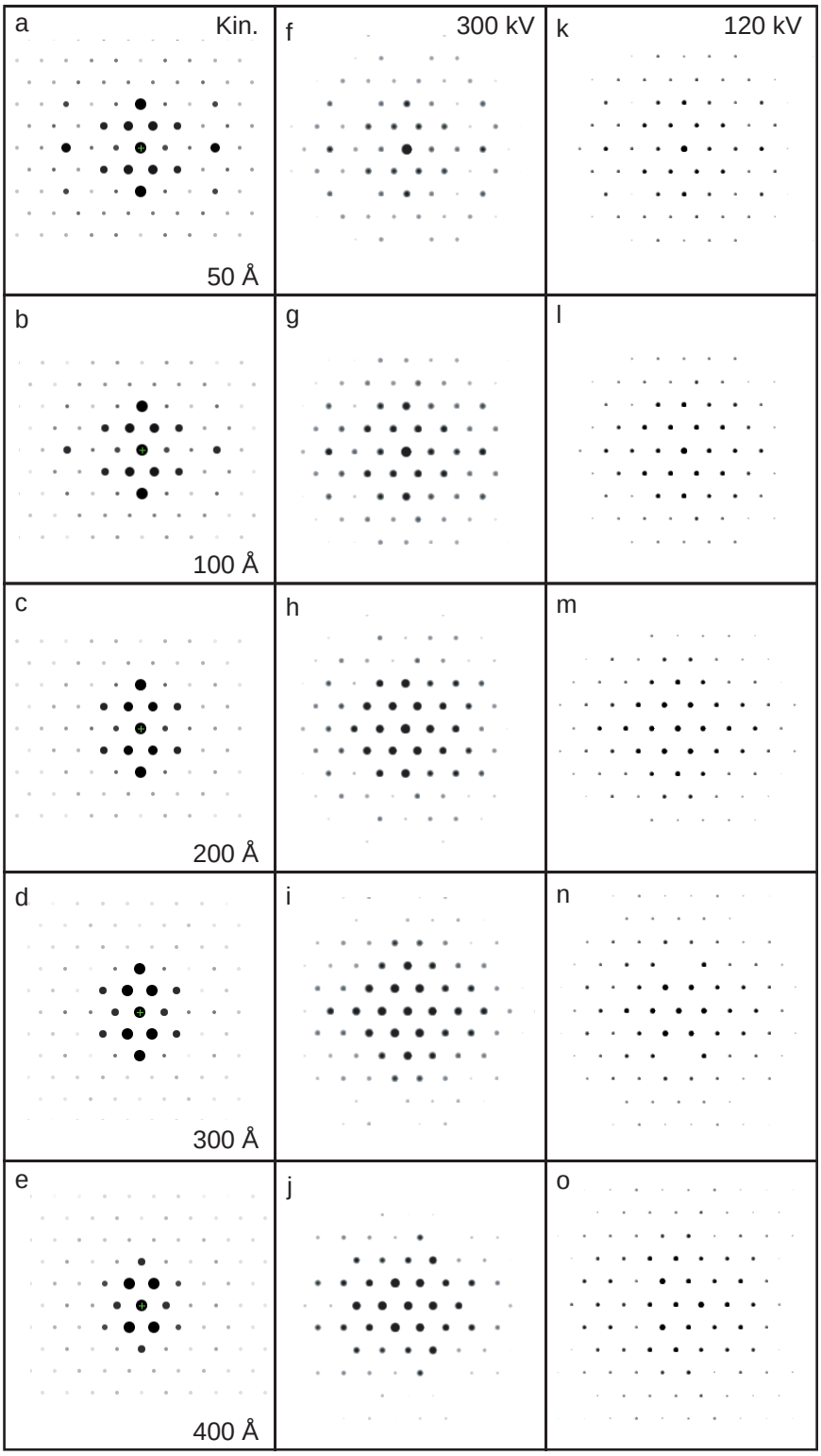

Fig OR1. ED patterns calculated along the [001] zone axis for cv-1*M* dioctahedral K-bearing aluminous mica. (a-e) Kinematical case; (f-j) dynamical case with Multislices method and 300 kV; (k-o) dynamical case with Multislices method and 120 kV.

Supplemental information for the paper (in *Physics and Chemistry of Minerals*)

"Polymorph and polytype identification of finely divided aluminous dioctahedral mica individual crystals with SAED. Kinematical and dynamical electron diffraction."

Anne-Claire Gaillot, Victor A. Drits, David R. Veblen, Bruno Lanson

Institut des Matériaux Jean Rouxel (IMN), Université de Nantes, CNRS, 2 rue de la Houssinière, BP 32229, 44322 Nantes Cedex 3, France - Anne-Claire.Gaillot@cnrs-imn.fr

Online Resource 2

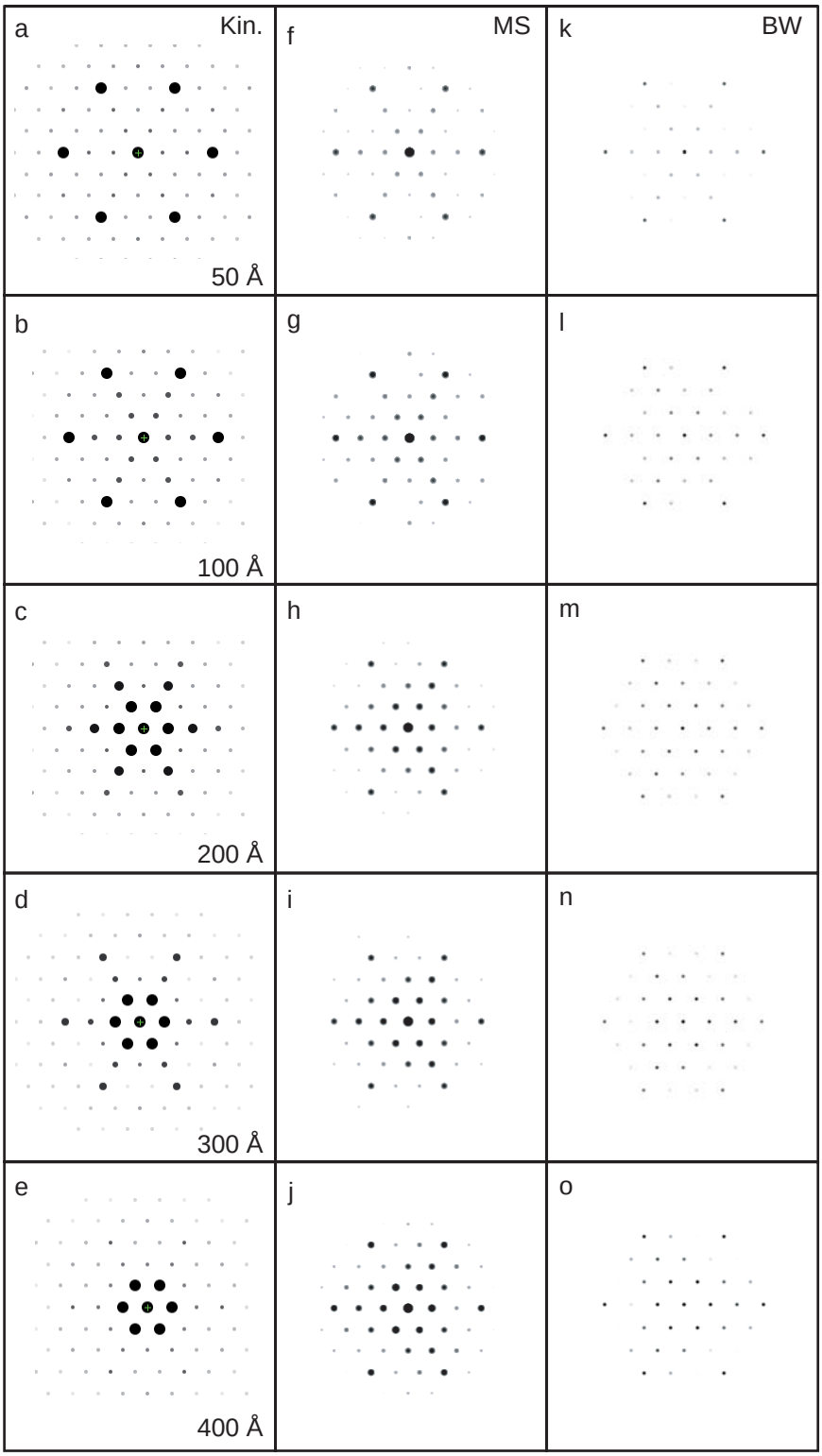

Fig OR2. ED patterns calculated along the [001] zone axis for 3*T* dioctahedral K-bearing aluminous mica. (a-e) Kinematical case; (f-j) dynamical case with Multislices method, 300 kV; (h-o) dynamical case with Blockwaves method, 300 kV.